Fuel 404 (2026) 136268

Contents lists available at ScienceDirect

Fuel

journal homepage: www.elsevier.com/locate/jfue

Full length article

Modelling nanoparticle deposition rate in iron particle combustion

Nils Hartmann [a], Andreas Kronenburg [a,*], Thorsten Zirwes [a], David Märker [b], Tien Duc Luu [b], Oliver Thomas Stein [b]

[a] Institute for Reactive Flows - University of Stuttgart, Pfaffenwaldring 31, Stuttgart, 70569, Germany
[b] Engler-Bunte-Institute Chair for Simulation of Reacting Thermo-Fluid Systems - Karlsruhe Institute of Technology, Engler-Bunte-Ring 7, Karlsruhe, 76131, Germany

HIGHLIGHTS

- Lagrangian and Eulerian simulations for nanoparticle deposition were compared.
- A single collector efficiency correlation accounting for Stefan flow was derived.
- An expression for the coagulation kernel for advection and Brownian diffusion was improved.
- A Coagulation kernel accounting for Stefan flow was derived.

ARTICLE INFO

Keywords:
Iron combustion
Nanoparticle deposition
Collector efficiency
Collision kernel

ABSTRACT

Iron powders attract increased interest as energy carrier as they can provide high temperature heat during combustion. The combustion products can be recycled using renewable energy leading to a carbon free and fully closed energy cycle. However, nanoparticles are formed as by-products. They are difficult to remove from the exhaust gases, and the slip of iron nanoparticles reduces cycle efficiency and compromises sustainability. Nanoparticle slip is reduced by their deposition onto the fuel microparticles that act as a spherical collector, but the fraction of the nanoparticles that do not escape due to deposition is totally unknown. In this study, Lagrangian and Eulerian simulations are performed to evaluate the deposition of nanoparticles onto microparticles due to inertial impaction and diffusion. The simulation results are validated with analytical solutions from the literature. Then, the effects of a positive and a negative Stefan flow occurring at the microparticle's surface during combustion are investigated. A model for the collection efficiency in the diffusion-dominated regime and in the presence of positive or a negative Stefan flows is proposed. This collection efficiency model can then be used to augment the classic kernel of Smoluchowski such that its validity is extended to flow conditions prevalent in iron combustion.

1. Introduction

As part of the Paris Agreement and subsequent conventions, many countries decided to reduce the emissions of greenhouse gases. One strategy to achieve climate goals is to use renewable energies for electricity production. However, renewable energy production using solar and/or wind energy is tied to geographic conditions and subject to significant variations within days, but in particular over the seasons. Therefore, matching the energy supply and demand requires transport and storage of energy from favorable production locations, with recyclable metal fuels emerging as an attractive storage medium, as they feature high power density and promise at least partial use of the existing energy infrastructure [1].

Metal powders provide high temperature heat during combustion and can be recycled using green hydrogen. Especially iron is an attractive metal, as it is an abundant material and an infrastructure for mining and transportation exists [1–3]. First experiments show promising results for the application of iron combustion [4,5], but also noted the formation of nanoparticles [4–12] that pose several challenges: nanoparticles are difficult to remove from the exhaust gases, resulting in emissions of particulate matter with uncertain effects on health and environment [13]. Moreover, nanoparticle slip, i.e., the loss of iron and its oxides with the

* Corresponding author.
Email addresses: nils.hartmann@irst.uni-stuttgart.de (N. Hartmann), kronenburg@irst.uni-stuttgart.de (A. Kronenburg), thorsten.zirwes@irst.uni-stuttgart.de (T. Zirwes), david.maerker@kit.edu (D. Märker), tien.luu@kit.edu (T.D. Luu), oliver.t.stein@kit.edu (O.T. Stein).

https://doi.org/10.1016/j.fuel.2025.136268
Received 10 March 2025; Received in revised form 30 June 2025; Accepted 12 July 2025
Available online 22 July 2025

exhaust gas, thwarts the idea of a fully closed and renewable energy cycle. It is therefore desirable to mitigate the formation of nanoparticles to reduce material and efficiency losses and/or to improve filter mechanisms for nanoparticle removal from the exhaust.

The iron fuel consists of particles in the micron range [9–12]. During combustion, heterogeneous reactions lead to a temperature increase, causing a small amount of iron and/or iron-oxides to evaporate. These gaseous iron species may undergo further reactions in the gas phase and eventually condense and nucleate to form nanoparticles [8,11,14,15]. Some particles adhere to the fuel microparticles after the combustion process [7,10–12]. Experiments suggest that the nanoparticles are formed upstream of the collecting microparticle [9]. The exact dynamics of the collision process vary as the oxidation reaction and the evaporation of iron species induce a Stefan flow [14–16]. This Stefan flow can dominate the bulk stream [17] and will therefore need to be included for the prediction of collisions between the nano- and microparticles and for estimates of the microparticle collection efficiency.

In general, the collection efficiency depends on various mechanisms such as diffusion, direct interception, inertial impaction, thermophoresis and interaction potentials. Limiting cases refer to conditions under which most of these mechanisms are negligible. This simplifies the mathematical description and the contribution of a single mechanism can be studied. In the context of iron combustion, diffusion and inertial impaction are considered to be the most important drivers for collisions between nanoparticles and the fuel particles, as will be discussed below. Among others, Levich [18] presented an analytic solution for the limiting case of pure diffusion. Langmuir [19] derived an analytic solution for the limiting case of inertial impaction. These two contributions can be combined to obtain a total collection efficiency, as proposed by Yao et al. [20]. Using numerical methods, various authors [21–23] derived more sophisticated single collector efficiency correlations. Although their work relates to groundwater filtration, the theory can be applied to some extent to nanoparticle collection in iron combustion.

Fundamentals of nanoparticle generation, transport and agglomeration/coagulation of similarly sized nanoparticles have been studied extensively [24]. These fundamentals are used in recent studies regarding nanoparticles, however, the deposition of nanoparticles onto microparticles, i.e., the collisions of nanoparticles with microparticles, is not yet described by a collision kernel [14,25,26].

Within the present study, the collection efficiency for nanoparticles onto microparticles, especially in the presence of Stefan flow, will be addressed and closures for the collision kernels that are needed for the modelling of the agglomeration process in a general dynamic equation for the population balance, are proposed. We investigate the collection of nanoparticles on a single microparticle that acts as a collector using two different numerical approaches: (1) An Eulerian reference frame, where the steady-state momentum and species transport equations are solved. The nanoparticles are modelled as a passive scalar subject to convection and diffusion while drag and inertia are omitted. This is commonly referred to as the dusty gas approach [27]. This approach is similar to the one used by Levich [18], who derived an analytical expression for the nanoparticle flow to the microparticle surface. Here, however, a numerical solution is sought that takes into account the evolution of a viscous boundary layer around the microparticle and does not assume Stokes flow. The Eulerian and analytical solutions are mainly used for validation of a second (Lagrangian) approach. (2) This Lagrangian approach is used to calculate the trajectories of discrete nanoparticles. This gives a more detailed description of nanoparticle collection, as drag and inertia of individual nanoparticles are accounted for. The collection of nanoparticles is evaluated from the number of nanoparticles colliding with the surface of the microparticle. A major advantage of this procedure is that the collision rate of nanoparticles with the microparticle can be directly obtained. Classical coagulation kernels are typically used for a statistical description of the coagulation process with the aid of the general dynamic equation. An improved kernel for collision frequencies in the presence of Stefan flow due to diffusion or evaporation is derived in the final section of this paper.

2. Methods

2.1. Governing equations - Eulerian framework

The steady-state equations for the conservation of mass and momentum,

$$\nabla \cdot \vec{u}_g = 0, \tag{1}$$

$$\nabla \cdot (\vec{u}_g \vec{u}_g) = \nu_g \nabla \cdot \nabla \vec{u}_g - \nabla \left(\frac{p}{\rho_g} \right), \tag{2}$$

are solved in combination with the passive scalar transport equation for the nanoparticle number density, n_{np},

$$\nabla \cdot (\vec{u}_g n_{np}) = \nabla \cdot (D_{np} \nabla n_{np}), \tag{3}$$

using the OpenFOAM solver simpleFoam. This approach assumes that the nanoparticles do not affect the gas velocity distribution, which is true for low nanoparticle number densities [24] that are to be expected in iron combustion [25]. The subscript 'g' refers to gas and 'np' to nanoparticle properties. Here, $\vec{u}_g$ is the velocity, ν_g the kinematic viscosity, ρ_g the density and p is the pressure. The nanoparticle diffusivity in the gas is governed by the Stokes-Einstein correlation

$$D_{np} = \frac{k_B T_g C^{slip}}{6\pi \mu_g (d_{np}/2)}, \tag{4}$$

where k_B is the Boltzmann constant, T_g the gas phase temperature (which is uniform within the entire domain but varies from case to case) and C^{slip} is the Cunningham correction factor [28]. The dynamic viscosity, μ_g, is taken as that of air and is a function of temperature.

We seek a solution for the rate of the number of nanoparticles collected by the microparticle, $\overline{J^S_{np}} = \int j^S_{np} \mathrm{d}A_{mp}$ with j^S_{np} being the nanoparticle flux normal to the microparticle surface, A_{mp}. The flux is composed of the diffusive and convective transport, $j^S_{np} = D_{np} \nabla n^S_{np} \cdot \vec{n} - u_s n^S_{np}$, with u_s denoting the velocity across the microparticle's surface due to Stefan flow that may either be positive due to evaporation or negative due to oxidation. Here, the definition of the normal vector $\vec{n}$ follows convention and points outwards from the microparticle surface. The nanoparticle number density on the microparticle surface and its gradient will be a function of inflow conditions and thermodynamic properties. Here, we use $\overline{J^S_{np}}$ rather than ∇n^S_{np} (or n^S_{np}) as independent variable, such that $\overline{J^S_{np}} = f(u_s, u_\infty, n_\infty, \mu_g, \rho_g, \nu_g, T_g, p, D_{np}, R_{mp})$, where the subscript '$mp$' refers to microparticle properties and '∞' to conditions far upstream from the microparticle surface, i.e., the inlet conditions. As $\overline{J^S_{np}}$ represents the integral over the microparticle surface, any spatial dependence has vanished. The variables ρ_g, μ_g and ν_g are related to each other and are functions of T_g. Equally, D_{np}, T_g and d_{np} are related by Eq. (4). Therefore, the functional dependence should include one material property for the gas phase only and two out of the three variables D_{np}, T_g and d_{np}. Pressure is taken to be constant and will not affect the collision efficiency. This leads to $\overline{J^S_{np}} = f(u_s, u_\infty, n_\infty, \nu_g, d_{np}, D_{np}, R_{mp})$ with three independent dimensions (length, time and particle number or concentration) and five dimensionless characteristic numbers. The Reynolds and Péclet numbers are defined as

$$\mathrm{Re}_\infty = 2u_\infty R_{mp}/\nu_g,$$

$$\mathrm{Pe}_\infty = 2u_\infty R_{mp}/D_{np},$$

and can be obtained from non-dimensionalization of Eqs. (2) and (3). Similarly, the Stefan flow at the microparticle surface and its effects

on the collection efficiency can be characterized by a Stefan Péclet number,

$$\mathrm{Pe}_S = |u_s| 2R_{mp}/D_{np}.$$

An interception number is given by

$$\mathrm{I} = d_{np}/(2R_{mp})$$

and relates the diameters of the nano- and microparticles. Here, however, I tends to be very small, interception due to finite nanoparticle diameter, d_{np}, is negligible and we assume the nanoparticles to be point particles in the Euler simulations [24]. Finally, a deposition efficiency, η, is the fifth characteristic variable. It is defined as the nanoparticle mass flow at the microparticle's surface normalized by the nanoparticle mass flow within the swept volume of the microparticle [29], viz.

$$\eta = \frac{\overline{J_{np}^S}}{n_\infty u_\infty \pi R_{mp}^2}. \tag{5}$$

This leads to a problem statement that can be expressed as $\eta = f(\mathrm{Re}_\infty, \mathrm{Pe}_\infty, \mathrm{Pe}_S)$ where η quantifies the nanoparticles that are collected by means of diffusion through a boundary layer. The latter is governed by the bulk flow velocity and the possible presence of Stefan flow across the microparticle surface.

The variables T_g (or rather v_g), u_∞, d_{np} and R_{mp} are varied within reasonable bounds to cover a wide range of Pe_∞ and Re_∞. The velocity at the microparticle surface resulting from the Stefan flow, u_s, is prescribed as detailed in Section 3.3. Note that Eq. (3) treats nanoparticles as a continuous phase without consideration of nanoparticle drag or inertia. This is similar to Levich [18], who derived an analytical solution for the total mass flow of nanoparticles to the microparticle surface assuming large Péclet and small Reynolds numbers. However, he assumed that there is no hydrodynamic boundary layer around the microparticle. In the present study, this assumption is dropped as flow displacement will affect nanoparticle collection and all boundary layers are fully resolved. Note that in the Lagrangian framework (Section 2.3) we will also drop the assumption of non-inertial particles. This introduces nanoparticle mass (or rather density) as an additional parameter and leads to one further characteristic quantity, the Stokes number (cf. Section 2.3).

For the case of Stokes flow without a hydrodynamic boundary layer, Levich [18] derived an analytical solution for the collection efficiency as,

$$\eta_0 = 4.03\mathrm{Pe}_\infty^{-2/3}. \tag{6}$$

Expression (6) will be used for comparison with our results below. The subscript '0' in Eq. (6) indicates the absence of Stefan flow.

2.2. Numerical setup - Eulerian framework

A symmetric three-dimensional geometry is used for the stationary, laminar flow around the microparticle. Fig. 1 shows a section of the domain with the velocity field depicted in the top half and the nanoparticle number density field in the bottom half. The spherical microparticle of constant radius R_{mp} is fixed in space and placed at the origin. The domain extends to $15R_{mp}$ upstream, downstream and in all cross-stream directions, such that the influence of the boundary conditions on the hydrodynamic and concentration boundary layers is well below 1 %. Only for cases with large Stefan flows directed outwards from the microparticle (strong evaporation), streamlines at the inlet would slightly diverge if a larger domain size were chosen. The error for these extreme cases can be estimated to be below 3 % for the inlet boundary being $15R_{mp}$ upstream of the microparticle. At the inlet, the velocity and nanoparticle number density are set to prescribed values u_∞ and n_∞, respectively. At the microparticle surface, the nanoparticle number density, n_{np}^S, is set to zero and the velocity, u_S, either to zero (no-slip boundary) in the absence of Stefan flow, or to a predetermined value (e.g., from relevant DNS [25]) in the case of a net diffusive flux towards the microparticle due to surface oxidation or away from the particle due to evaporation. A total of approximately 1.5×10^6 cells with radial grading at the microparticle surface ensures mesh independence of the results and has been used for all computations. This results in a cell size of $\Delta \approx 0.25R_{mp}$ at the microparticle surface to fully resolve the hydrodynamic and concentration boundary layers.

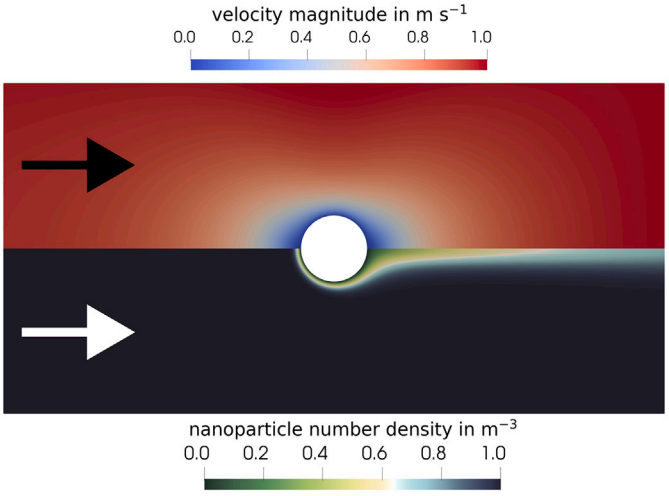

Fig. 1. Section of the domain used for the Eulerian framework with inflow on the left and the microparticle in the centre. The velocity field is shown in the top half and the nanoparticle number density field in the bottom half. The principal flow direction is indicated by the arrows.

2.3. Governing equations - Lagrangian framework

In the Lagrangian framework, the nanoparticles are considered to be discrete entities and their motion is governed by the Langevin equation,

$$m\frac{\mathrm{d}\vec{u}_{np}}{\mathrm{d}t} = \vec{F}_d + \vec{F}_b. \tag{7}$$

The drag force, $\vec{F}_d$, is given by

$$\vec{F}_d = -f\vec{u}_{rel} = \frac{6\pi\mu_g(d_{np}/2)}{C^{slip}}\vec{u}_{rel}, \tag{8}$$

where the model for the friction coefficient, f, assumes a spherical shape of the nanoparticle and follows Stokes' law. The variable $\vec{u}_{rel} = \vec{u}_{np} - \vec{u}_g$ denotes the relative velocity between the nanoparticle and the gas. In contrast to the nanoparticle description in the Eulerian framework (Eq. 3), the Langevin equation includes the nanoparticle mass, m, and considers drag/friction. This additional dependence on mass, or rather nanoparticle density ρ_{np}, gives rise to a further dimensionless group, the Stokes number [24],

$$\mathrm{St}_\infty = \left[\rho_{np} d_{np}^2\, C^{slip}/(18\mu_g)\right] u_\infty/R_{mp},$$

that characterizes the system. The Brownian force, $\vec{F}_b$, is given by

$$\vec{F}_b = \sqrt{\frac{2\, f k_B T_g}{\Delta t}}\vec{G}, \tag{9}$$

where Δt is the numerical time step and $\vec{G}$ is a vector containing random variables sampled from a Gaussian distribution with zero mean and unity variance. The Langevin equation (7) is numerically integrated using the Leapfrog algorithm in OpenFOAM [30].

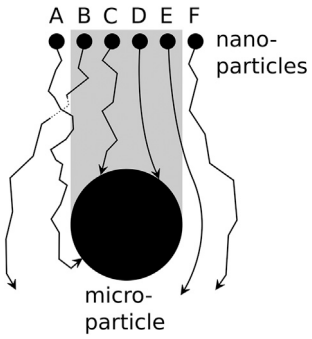

Fig. 2. Depiction of the collection efficiency by means of possible nanoparticle trajectories (A–F). The swept volume is indicated by the grey area.

The definition of the collection efficiency is adapted from Eq. (5) to give

$$\eta = \frac{N_{np}\,\text{collected}}{n_\infty \times \text{swept volume}}, \tag{10}$$

with N_{np} being the number of nanoparticles. Fig. 2 provides a visual description of the collection efficiency as given by Eq. (10) and illustrates possible outcomes for the nanoparticle trajectories in the Lagrangian framework. The swept volume is marked by the grey area. In general, the trajectories always follow a random path due to Brownian motion, but the deterministic advective transport may dominate for nanoparticles with high inertia. For the case of diffusion-dominant processes with low inertia, particles from outside the swept volume may diffuse towards the microparticle (A) or may pass it due to divergent streamlines around the microparticle (F). Similarly, particles from within the swept volume may collide with the microparticle (C, D) or pass the microparticle without collision (B, E). It is important to note that a Stefan flow modifies the streamlines and thus the trajectories of the nanoparticles. A negative Stefan flow is induced by the heterogeneous reactions at the microparticle surface due to oxygen diffusion and consumption at the microparticle interface [14–16]. This Stefan flow is directed towards the microparticle surface and can dominate the overall flow field in the vicinity of the microparticle [17]. The index '*O*' for oxidation is used to refer to such a case of a negative Stefan flow. Then, the efficiency may be greater than 100 % ($\eta_O > 1$), as the negative Stefan flow is advecting nanoparticles from outside the swept volume towards the microparticle surface. Alternatively, a positive Stefan flow can be induced by evaporating species at high microparticle temperatures and has the opposite effect [15]. For sufficiently high evaporation rates, the positive Stefan flow will dominate and result in a net flow pointing away from the microparticle surface. The index '*E*' for evaporation is used to refer to the case of a positive Stefan flow. For a fully oxidized microparticle, surface oxidation and evaporation stop and Stefan flow is no longer present (index '0'). In systems with multiple microparticles like iron combustion, microparticles in either of these states (O, E or 0) may be present at the same time [17,31].

2.4. Numerical setup - Lagrangian framework

The general concept of the Lagrangian framework is depicted in Fig. 3. Nanoparticles, represented by the black dots, move towards the microparticle due to advection. The computational domain and mesh are identical to the Eulerian framework, which is still used to obtain the velocity field as indicated by the streamlines (cf. Section 2.2). The integration time step is set to $\Delta t = 1 \times 10^{-7}$ s, which is smaller than the nanoparticle relaxation time, $\Delta t < \tau^{relax} = \rho_{np} d_{np}^2\, C^{slip}/(18\mu_g)$, for all simulations.

The boundary conditions for the nanoparticles are set to mimic the boundary conditions for the Eulerian framework as described in Section 2.2. At the inlet, a constant nanoparticle flow rate of monosized nanoparticles with a statistically uniform, but random distribution, is imposed. The collection efficiency (Eq. 10) was evaluated using a total of 2×10^6 nanoparticles. This particle number ensures statistical convergence to within 0.5 % for the vast majority of results. An exception is cases with strong evaporation. Here, uncertainties of up to 5 % can be observed as collision efficiencies decrease by up to two orders of magnitude and the reliability of the statistics deteriorates due to the low number of collisions. The nanoparticles adhere to the microparticle surface upon contact but do not affect nearby nanoparticles nor the microparticle surface in any way, as they are very small compared to the microparticle and do not contribute to notable growth and thus increases in collector surface. This approach implicitly assumes one-way coupling, where the nanoparticles do not affect the gas stream or each other. Outflow boundary conditions are applied at the sides and at the outlet plane. The initial nanoparticle velocities are set equal to the gas velocity, i.e., the drag force (Eq. 8) is zero, initially. For positive Stefan flow that represents evaporation and a net mass flow from the microparticle surface to the surroundings, the streamlines originate on the microparticle surface. This is shown in the top half of Fig. 4. Streamlines are no longer tangent to the microparticle surface. This is similar for the case of negative Stefan flow, referring to oxidation and a net mass flow towards the particle as depicted in the bottom half of Fig. 4. The streamlines are

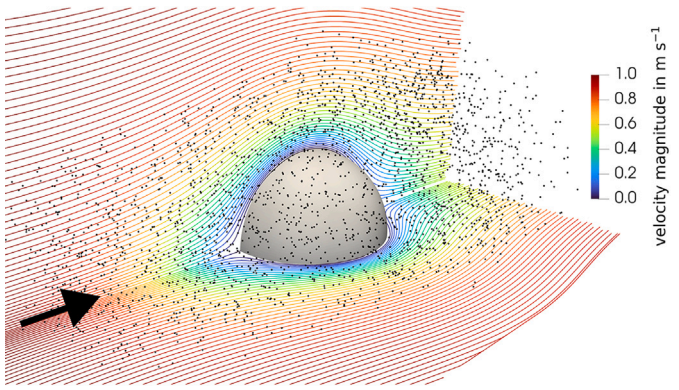

Fig. 3. Visualization of the Lagrangian setup. The gas flow is indicated by the streamlines. The direction of the gas flow is given by the arrow from front to rear. For clarity of presentation, only a quarter of the domain is shown and the number of nanoparticles is reduced. They are represented by dots with an arbitrary diameter for clarity of presentation.

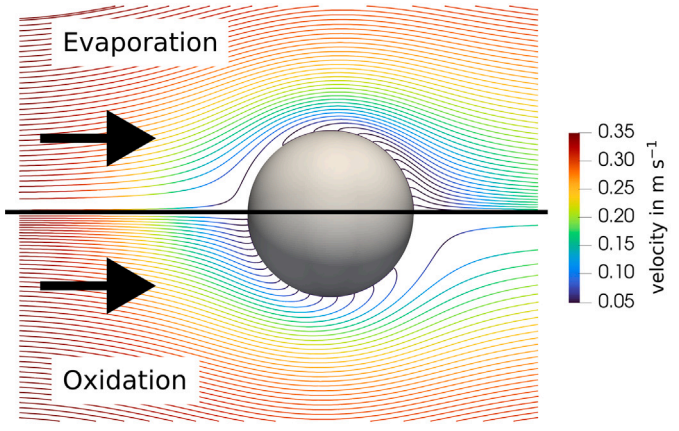

Fig. 4. Gas flow around the microparticle with Stefan flow, indicated by streamlines. The Stefan flow is positive for evaporation (top half) and negative for oxidation (bottom half). The bulk flow direction is given by the arrows.

directed towards the microparticle surface, instead of originating there. However, independent of the direction of Stefan flow, the velocity magnitude at the microparticle surface is not zero. The no-slip boundary condition no longer holds and a velocity or mass flow rate across the microparticle surface needs to be prescribed.

3. Results and discussion

3.1. Diffusion-dominated regime

We first investigate collection efficiencies in the diffusion-dominated regime in the absence of Stefan flow, i.e., we set $Pe_s = 0$. Process conditions that are typical for iron combustion are listed in Table 1. The table also includes the relevant references where these ranges are specified and provides limits of the characteristic numbers associated with the process conditions.

Fig. 5 compares the collection efficiencies from the Euler and Lagrange simulations across a wide range of these process conditions. We note that the Eulerian and Lagrangian solutions almost perfectly match. This is expected as the Lagrangian approach should recover the pure diffusion process for sufficiently long particle relaxation times, if the definition of the Brownian force is consistent with the definition of the nanoparticle diffusion coefficient. As all Stokes numbers are below 0.1, inertia will not play a major role in the collection of the nanoparticles [19]. Since $d_{np}/2 << R_{mp}$, collection by interception is negligible [29]. Likewise, interaction potentials between nanoparticles are negligible, as conditions are assumed to be dilute [25,33]. Thermophoresis or temperature gradients in general are omitted here for direct comparison to the analytical solutions. Consequently, the collection of nanoparticles is only due to diffusion to the microparticle surface (which justifies the characterization as "diffusion-dominated collection" even for very large Pe_∞) and a simple convection-diffusion process suffices to approximate the collector efficiency. The black line in Fig. 5 is a suitable fit to the simulation results and is given by

$$\eta_0 = 4.4 Pe_\infty^{-2/3}. \tag{11}$$

The analytical solution by Levich [18] (Eq. 6) is also included in Fig. 5 which gives a prediction about 9.2 % below the simulation data across the entire Péclet number range. Similar deviations from Levich's solution are also seen in the numerical results from different authors [21–23] and are attributed to the influence of the hydrodynamic boundary layer which is neglected in the original solution [21]. An optimal fit to the simulations would be $\eta_0 = 4.74 Pe_\infty^{-0.676}$, but differences from our model (Eq. 11) are less than 3 % for the cases presented here. We therefore advocate a '-2/3'-dependence as it provides a good approximation (with a coefficient of determination of $R^2 = 0.998$) and agrees with theory.

Table 1
Parameter range representing typical process conditions in iron combustion. The dimensionless numbers indicate the range that variation of the parameters covers.

Variable	Value	Reference
R_{mp}	5.67–80 µm	[9–12]
d_{np}	20–200 nm	[4,10,14]
T_g	1500–2700 K	[8,12,14–16,32]
u_∞	<1.25 m s^{-1}	[9]
ρ_{np}	5100–5277 kg m^{-3}	[10,14]
Re_∞	<0.83	
Pe_∞	<167 150	
I	1.24×10^{-4} – 0.018	

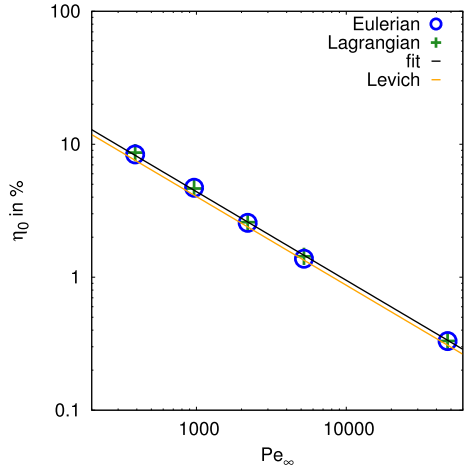

Fig. 5. Results of the numerical frameworks in comparison to the analytical solution of Levich [18]. The black line is a best fit through the simulation data preserving the trend $\eta_0 \sim Pe_\infty^{-2/3}$. The Stokes numbers are $St_\infty \leq 0.1$ here. (For interpretation of the references to colour in this figure legend, the reader is referred to the web version of this article.)

3.2. Effects of inertia

The literature on iron microparticle combustion suggests the largest Stokes number to be around $St_\infty = 0.34$. This value is still below the critical Stokes number $St_{\infty,c} = 1.214$ evaluated by Langmuir [19], indicating that inertial impaction is not contributing to the collection efficiency. However, Mora and Rosner [34] showed that inertial effects for $0.3 < St_\infty < 1.214$ enhance the collection by diffusion significantly. Inertia at subcritical Stokes numbers can lead to a local increase in the nanoparticle number density near the forward stagnation point of the microparticle [34,35]. Here, we extend the Stokes number range from 0.1 up to 10 while holding the Péclet number constant at around $Pe_\infty \approx 20000$. This would correspond to rather large nanoparticles, small microparticles and/or high relative velocities between gas and microparticle and serves here primarily for an assessment of the transition regime where low Stokes number assumptions break down. The results are given in Fig. 6, where the Lagrangian and Eulerian frameworks are compared with an analytical solution that is given by $\eta_0 = \eta_D + \eta_I$, following the approach of additivity of Yao [20]. The collection efficiency due to diffusion, η_D, is taken from Levich [18] (Eq. 6) and the collection efficiency due to inertial impaction, $\eta_I = [1 + 3/4 \ln(2\,St_\infty)/(St_\infty - 1.214)]^{-2}$, is taken from Langmuir [19]. Three Stokes number ranges can be identified in Fig. 6:

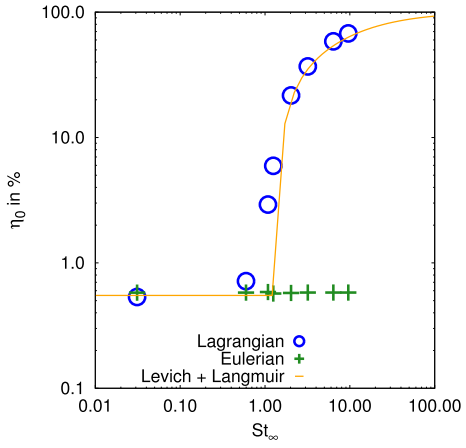

Fig. 6. Results of the numerical frameworks in comparison to the approach of Yao et al. [20], i.e. the superposition of the solutions of Levich [18] and Langmuir [19]. The Péclet number is constant at $Pe_\infty \approx 20000$.

1. $St_\infty \leq 0.1$: This is the diffusion-dominated regime, where η_0 is constant for constant Pe_∞ (cf. Section 3.1).
2. $0.1 < St_\infty \leq 1.214$: The Eulerian and analytical solutions remain constant while the Lagrangian solution shows a continuous increase in η_0. The growth appears to be exponential for $St > 0.3$, which is in accordance with the findings of Mora and Rosner [34]. The increase levels off at $St_{\infty,c} = 1.214$.
3. $St_\infty > 1.214$: This is the inertia-dominated regime. Again, the Eulerian framework cannot account for an increase in collection efficiency as it disregards effects of inertia. The analytical solution, however, features a steep increase at the critical Stokes number and asymptotes towards 100 % for very large St_∞. The Lagrangian solution converges with the analytical solution for $St_\infty = 10$. We note that the Lagrangian framework provides a suitable transition behaviour between the two limits of diffusion- and inertia-dominated regimes.

3.3. Impact of Stefan flow in the diffusion-dominated regime

The velocity at the microparticle surface resulting from the Stefan flow, u_s, is prescribed and accounts for mass flows to and from the microparticle due to surface oxidation and evaporation, respectively. For positive Stefan flows, the maximum value of u_s is chosen as the limit where the collection efficiency is almost zero, $\eta_E \approx 0$, which differs for every Péclet number, Pe_∞. For negative Stefan flows it is varied down to $u_s = -0.2$ m s^{-1}. Fig. 7 shows the collection efficiency referring to a positive Stefan flow (evaporation) for a range of Péclet numbers Pe_∞ and Stefan Péclet numbers Pe_S. The collection efficiencies η_E for evaporation are normalized with the reference value η_0 (Eq. 11). They then scale well with the eighth power of the Stefan Péclet number,

$$(\eta_E/\eta_0)^{1/8} \propto Pe_S, \tag{12}$$

where the proportionally factor or slope, m_E, is a strong function of the Péclet number and can be approximated by

$$m_E = -\frac{1}{15} Pe_\infty^{-1/3}. \tag{13}$$

Based on our simulation data, the collection efficiency for evaporation can be modelled as

$$\eta_E = (1 + m_E Pe_S)^8 \eta_0 = \left(1 - \frac{1}{15}\frac{Pe_S}{Pe_\infty^{1/3}}\right)^8 4.4 Pe_\infty^{-2/3}. \tag{14}$$

Eq. (14) is represented in Fig. 7 by the black lines. Similarly, the collection efficiency for a negative Stefan flow (oxidation) can be modelled as

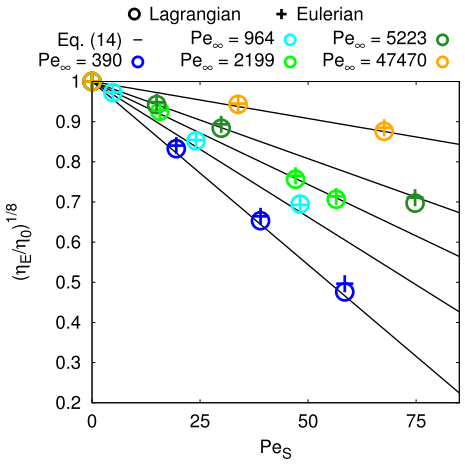

Fig. 7. Results of the numerical frameworks and the collection efficiency model for **evaporation** (positive Stefan flow) (Eq. 14).

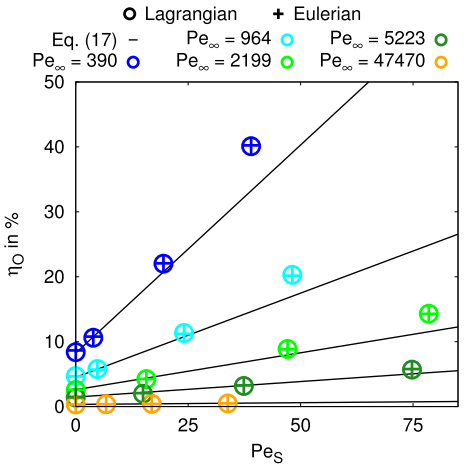

Fig. 8. Results of the numerical frameworks and the collection efficiency model for **oxidation** (negative Stefan flow) (Eq. 17).

a function of the Stefan Péclet number. Fig. 8 shows, however, a linear dependence for a range of Péclet numbers and Stefan Péclet numbers,

$$\eta_O \propto Pe_S. \tag{15}$$

The slope can be approximated by

$$m_O = 2.5 Pe_\infty^{-1}. \tag{16}$$

The collection efficiency for oxidation is modelled as

$$\begin{aligned}\eta_O &= m_O Pe_S + \eta_0 \\ &= 2.5\frac{Pe_S}{Pe_\infty} + 4.4 Pe_\infty^{-2/3}.\end{aligned} \tag{17}$$

Eq. (17) is represented in Fig. 8 by the black lines.

In general, we observe a good agreement between the evaporation model given by Eq. (14) and the simulations for the whole range of Stefan Péclet numbers ($R^2 < 0.999$). Deviations occur mainly when $Pe_S \approx 0.0$ (see Section 3.1) and approach zero elsewhere. Evaporation will enlarge the diffusion boundary layer as nanoparticles are transported away from the microparticle surface by means of the advective Stefan flow. Strong evaporation will therefore lead to a collection efficiency approximating 0 %, which is taken into account by the model (Eq. 14). The predictions by the oxidation model depicted in Fig. 8 and given by Eq. (17) agree well with the numerical solutions ($R^2 < 0.955$), but deviations grow when the negative Stefan flow dominates, meaning Péclet numbers approximately reach $Pe_S \approx 1/2 Pe_\infty$. These large Pe_S correspond to strong oxidation (large values of u_S) where all streamlines in the vicinity of the microparticle terminate on its surface. Then, the flow rate towards the microparticle surface, $\overline{J_{np}^S} = n_{np}^S u_S A_{mp}$, determines the number of nanoparticles collected and collection by ordinary diffusion becomes negligible, i.e., the collection efficiency as defined by Eqs. (5) and (10) ceases to be meaningful. In this case the collection efficiency is given by $\eta_O = \overline{J_{np}^S}/(n_\infty u_\infty \pi R_{mp}^2)$, which results in $\eta_O = 4 Pe_S/Pe_\infty$, when $n_{np}^S = n_\infty$ due to the dominant negative Stefan flow during strong oxidation.

3.4. Collision kernels

The results provided in Section 3.3 can be used to derive a model for the collision kernel that would be needed in a statistical description of the collision process. The evolution of a particle size distribution,

$n(v)$, with particle volume v, is governed by the general dynamic equation

$$\frac{\partial n}{\partial t} + \frac{\partial n\dot{v}}{\partial v} = \frac{1}{2}\int_0^v \beta(v-v', v')n(v-v')n(v')\mathrm{d}v' - \int_0^\infty \beta(v, v')n(v)n(v')\mathrm{d}v + \delta_n, \tag{18}$$

assuming a homogeneous particle distribution, the absence of any source or sink and no external forces [24]. The second LHS-term is a drift term in v-space due to, e.g., surface growth and the two RHS-terms represent an increase (first term) and decrease (second term) in number density of particles of size v due to particle collision. β is the collision frequency that accounts for the number of collisions per time and needs to be modelled. Eq. (18) may be further simplified to

$$\frac{\partial n_{np}}{\partial t} = -\beta n_{np} n_{mp}, \tag{19}$$

by invoking additional assumptions that are applicable in the case of iron combustion with a bi-disperse population consisting of nano- and microparticles only. We assume a dilute system without collisions and growth of nanoparticle agglomerates and microparticles being much larger than the nanoparticles such that deposition of nanoparticles on the collector does not modify the collector's size. Smoluchowski [36] derived a collision kernel for the continuum regime,

$$\beta_{SM} = 4\pi(D_{mp} + D_{np})(R_{mp} + d_{np}/2), \tag{20}$$

for the collisions between differently sized particles of spherical shape. Smoluchowski's kernel can be simplified for large microparticles with a relatively low diffusion coefficient ($D_{np} \gg D_{mp}$ and $d_{np}/2 \ll R_{mp}$) to give

$$\beta_{SM} = 4\pi D_{np} R_{mp}. \tag{21}$$

However, this kernel assumes collisions due to Brownian motion and neglects inertial effects such that its applicability to iron combustion with particle sizes of the order of tens of micrometres is unlikely, and the true collision efficiencies will notably deviate from Eq. (21) for larger Péclet numbers [18]. The number of collisions between micro- and nanoparticles, Z_{coll}, is obtained from the Lagrangian simulation and is related to the number of collisions per volume and time, z_{coll}, by

$$z_{coll} = \frac{Z_{coll}}{\Delta t V} = u_\infty \pi R_{mp}^2 \eta_0 n_{np} \frac{N_{mp}}{V}, \tag{22}$$

where V is the volume of the domain and N_{mp} is the number of microparticles within this volume, $N_{mp}/V = n_{mp}$. Comparison of Eqs. (19) and (22) then yields

$$\beta = u_\infty \pi R_{mp}^2 \eta_0. \tag{23}$$

The right-hand-side of this equation can be expanded using Smoluchowski's kernel from Eq. (21) to yield

$$\beta = \frac{u_\infty \pi R_{mp}^2}{4\pi D R_{mp}} \eta_0 \beta_{SM} = \frac{1}{8}\mathrm{Pe}_\infty \eta_0 \beta_{SM}. \tag{24}$$

This may be rewritten in terms of a Sherwood number, as common in mass transfer theory. Considering the nanoparticle flux at the microparticle surface and applying the Smoluchowski-Levich approximation of a perfect sink, it can be approximated by

$$\dot{n}''_{np} = \frac{n_{np} u_\infty \pi \cancel{R_{mp}^2} \eta_0}{4\pi \cancel{R_{mp}^2}} = k(n_{np} - \overset{0}{\cancel{n^s_{np}}}), \tag{25}$$
$$\rightarrow k = u_\infty \eta_0,$$

where k is the mass transfer coefficient. The Sherwood number can then be obtained from

$$\mathrm{Sh}_\infty = \frac{2kR_{mp}}{D_{np}} = \frac{1}{4}\eta_0 \mathrm{Pe}_\infty. \tag{26}$$

Inserting this into Eq. (24) gives

$$\beta = \frac{\mathrm{Sh}_\infty}{2}\beta_{SM}. \tag{27}$$

This is equivalent to Levich [18] with the difference of a 9.2 % higher collector efficiency implied by our modelling of η_0. The collision model (Eqs. 26 and 27) is extended to evaporation and oxidation by replacing η_0 with η_E (Eq. 14) and η_O (Eq. 17), respectively. In Fig. 9, the Lagrangian results and the collision model (Eq. 27) are compared for a representative (moderate) Péclet number of $\mathrm{Pe}_\infty = 964$. For evaporation, depicted in Fig. 9(a), the collision model gives good predictions over the whole range of Stefan Péclet numbers. However, for strong oxidation depicted in Fig. 9(b), the model becomes less accurate, which is a consequence of the modelling of the collection efficiency (cf. Section 3.3). A comparison to the classical kernel of Smoluchowski [36] considering Brownian coagulation only, shows that advection and Stefan flow have a significant impact on the collision rate in iron combustion, which is accounted for via the Sherwood number in our collision model (Eq. 27). Fig. 10 shows the Lagrangian solution and the collision model (Eq. 27) for a higher Péclet number of $\mathrm{Pe}_\infty = 5223$ for comparison. Here again, the model is accurate for evaporation, but deviations increase for strong oxidation. The validity of expression (27) is limited, however, to low microparticle number densities where the swept volumes of different microparticles

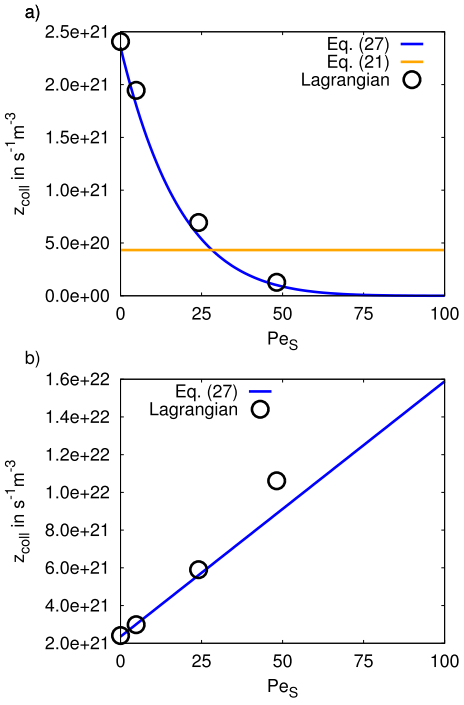

Fig. 9. Lagrangian solution and the model for evaporation in a) and for oxidation in b) for a moderate Péclet number of $\mathrm{Pe}_\infty = 964$. The kernel of Smoluchowski [36] (Eq. 21) is also included in a) for reference. Eqs. (21) and (27) are multiplied with the number densities according to Eq. (19).

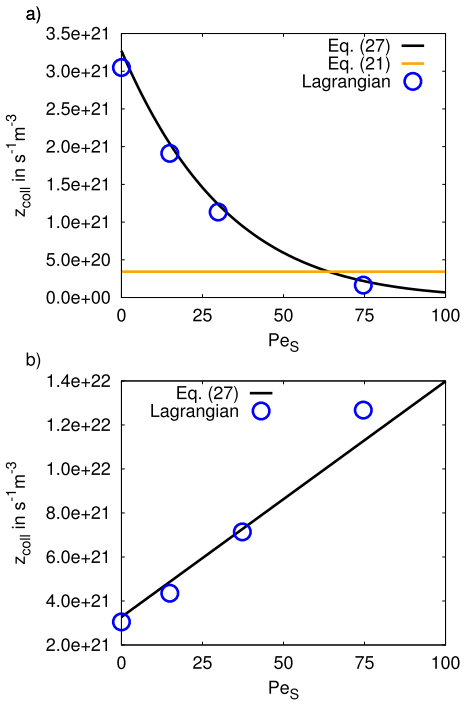

Fig. 10. Lagrangian solution and the model for evaporation (Eq. 27) in a) and for oxidation in b) for a high Péclet number of $Pe_\infty = 5223$. The kernel of Smoluchowski [36] (Eq. 21) is additionally included in a). Eqs. (21) and (27) are multiplied with the number densities according to Eq. (19).

are sufficiently resolved by the computational mesh such that the local nanoparticle number density upstream of the microparticle is known.

4. Conclusion

In this study, we have investigated the collection of nanoparticles onto a single microparticle using Lagrangian and Eulerian simulations. The conditions in terms of nanoparticle and microparticle size, relative velocity and gas phase properties have been chosen to cover a wide range of process parameters such that they are representative of iron particle combustion.

We have found that the simulations yield a collection efficiency 9.2 % higher than the analytic solution of Levich [18] for the diffusion-dominated regime. Additionally, effects of nanoparticle inertia on the collection efficiency have been investigated with the Lagrangian simulations; they have confirmed the sub-critical effects described by Mora and Rosner [34] and have converged against the analytic solution of Langmuir [19] for large Stokes numbers. The investigations of the collection efficiency have been extended to account for the presence of positive or negative Stefan flows and a model based on an adapted collector efficiency is proposed. This collector efficiency can also be applied for the modelling of a collision kernel that is typically used in a statistical approach such as the solution of the generalized dynamic equation for the evolution of nanoparticle size distributions. The new collision kernel can be expressed as an expansion of the classic kernel from Smoluchowski [36] where the effects of the advective flow can be accounted for via a suitably defined Sherwood number. This expansion holds for flows with and without Stefan flow. We refer, however, to future work with respect to the effects of variable thermodynamic properties and thermophoresis. In the present paper, we have assumed constant temperatures for an unbiased comparison to analytic solutions, but temperature gradients around the particle are expected to be large and thermophoretic effects will not be negligible in real iron combustion processes as they are likely to significantly affect the nanoparticle collection efficiency [37]. It is also noted that Pe_S will vary with time as oxidation of microparticles will first induce a negative Stefan flow while subsequent nanoparticle evaporation will induce a positive flow. It needs to be assessed whether quasi-steady states can be assumed, whether the models developed here can be applied to time sequences and how accurately they perform.

CRediT authorship contribution statement

Nils Hartmann: Writing – original draft, Visualization, Validation, Software, Methodology, Investigation, Formal analysis, Data curation, Conceptualization. **Andreas Kronenburg:** Writing – review & editing, Supervision, Resources, Project administration, Methodology, Funding acquisition, Formal analysis, Conceptualization. **Thorsten Zirwes:** Writing – review & editing, Validation, Software, Methodology, Investigation. **David Märker:** Writing – review & editing, Validation. **Tien Duc Luu:** Writing – review & editing, Investigation. **Oliver Thomas Stein:** Writing – review & editing, Funding acquisition, Conceptualization.

Declaration of competing interest

The authors declare that they have no known competing financial interests or personal relationships that could have appeared to influence the work reported in this paper.

Acknowledgements

This work was supported by the Friedrich and Elisabeth Boysen-Stiftung, project BOY-195. O.T. Stein gratefully acknowledges the financial support by the Helmholtz Association of German Research Centres (HGF), within the research field Energy, program Materials and Technologies for the Energy Transition (MTET).

Data availability

Data will be made available upon reasonable request.

References

[1] Bergthorson JM. Recyclable metal fuels for clean and compact zero-carbon power. Prog Energy Combust Sci 2018;68:169–96.
[2] Bergthorson JM, Goroshin S, Soo MJ, Julien P, Palecka J, Frost DL, et al. Direct combustion of recyclable metal fuels for zero-carbon heat and power. Appl Energy 2015;160:368–82.
[3] Debiagi P, Rocha RC, Scholtissek A, Janicka J, Hasse C. Iron as a sustainable chemical carrier of renewable energy: analysis of opportunities and challenges for retrofitting coal-fired power plants. Renew Sustain Energy Rev 2022;165:112579.
[4] Wiinikka H, Vikström T, Wennebro J, Toth P, Sepman A. Pulverized sponge iron, a zero-carbon and clean substitute for fossil coal in energy applications. Energy Fuels 2018;32(9):9982–9.
[5] Fedoryk M, Stelzner B, Harth S, Trimis D. Experimental investigation of the laminar burning velocity of iron-air flames in a tube burner. Appl Energy Combust Sci 2023;13:100111.
[6] Tóth P, Ögren Y, Sepman A, Gren P, Wiinikka H. Combustion behavior of pulverized sponge iron as a recyclable electrofuel. Powder Technol 2020;373:210–9.
[7] Panahi A, Chang D, Schiemann M, Fujinawa A, Mi X, Bergthorson JM, et al. Combustion behavior of single iron particles-part I: an experimental study in a drop-tube furnace under high heating rates and high temperatures. Appl Energy Combust Sci 2023;13:100097.
[8] Ning D, Shoshin Y, van Oijen JA, Finotello G, de Goey LP. Critical temperature for nanoparticle cloud formation during combustion of single micron-sized iron particle. Combust Flame 2022;244:112296.
[9] Li T, Heck F, Reinauer F, Böhm B, Dreizler A. Visualizing particle melting and nanoparticle formation during single iron particle oxidation with multi-parameter optical diagnostics. Combust Flame 2022;245:112357.
[10] Buchheiser S, Deutschmann MP, Rhein F, Allmang A, Fedoryk M, Stelzner B, et al. Particle and phase analysis of combusted iron particles for energy storage and release. Materials 2023;16(5):2009.
[11] Ning D, Shoshin Y, van Stiphout M, van Oijen J, Finotello G, de Goey P. Temperature and phase transitions of laser-ignited single iron particle. Combust Flame 2022;236:111801.
[12] Li S, Huang J, Weng W, Qian Y, Lu X, Aldén M, et al. Ignition and combustion behavior of single micron-sized iron particle in hot gas flow. Combust Flame 2022;241:112099.
[13] Wen D. Nanofuel as a potential secondary energy carrier. Energy Environ Sci 2010;3(5):591–600.

[14] Thijs LC, van Gool CEAG, Ramaekers WJS, van Oijen JA, de Goey LPH. Resolved simulations of single iron particle combustion and the release of nano-particles. Proc Combust Inst 2023;39(3):3551–9.
[15] Mich J, da Silva AK, Ning D, Li T, Raabe D, Böhm B, et al. Modeling the oxidation of iron microparticles during the reactive cooling phase. Proc Combust Inst 2024;40(1):105538.
[16] Nguyen B-D, Braig D, Scholtissek A, Ning D, Li T, Dreizler A, et al. Ignition and kinetic-limited oxidation analysis of single iron microparticles in hot laminar flows. Fuel 2024;371:131866.
[17] Vance FH, Scholtissek A, Nicolai H, Hasse C. Flame propagation modes for iron particle clusters in air, part II: transition from continuous to discrete propagation mode under strong convection effects. Combust Flame 2024;265:113199.
[18] Levich VG. Physicochemical hydrodynamics, Prentice-Hall international series in the physical and chemical engineering sciences. Prentice-Hall; 1962.
[19] Langmuir I. The production of rain by a chain reaction in cumulus clouds at temperatures above freezing. J Atmos Sci 1948;5(5):175–92.
[20] Yao K-M, Habibian MT, O'Melia CR. Water and waste water filtration. Concepts and applications. Environ Sci Technol 1971;5(11):1105–12.
[21] Tufenkji N, Elimelech M. Correlation equation for predicting single-collector efficiency in physicochemical filtration in saturated porous media. Environ Sci Technol 2004;38(2):529–36.
[22] Messina F, Marchisio DL, Sethi R. An extended and total flux normalized correlation equation for predicting single-collector efficiency. J Colloid Interface Sci 2015;446:185–93.
[23] Nelson KE, Ginn TR. New collector efficiency equation for colloid filtration in both natural and engineered flow conditions. Water Resour Res 2011;47(5).
[24] Friedlander SK. Smoke, dust, and haze: fundamentals of aerosol dynamics. Topics in chemical engineering. Oxford University Press; 2000.
[25] Nguyen B-D, Scholtissek A, Li T, Ning D, Stein OT, Dreizler A, et al. Nanoparticle formation in the boundary layer of burning iron microparticles: modeling and simulation. Chem Eng J 2025;507:160039.
[26] Finke J, Sewerin F. A population balance approach for predicting the size distribution of oxide smoke near a burning aluminum particle. Combust Flame 2024;265:113464.
[27] Balachandar S, Eaton JK. Turbulent dispersed multiphase flow. Annu Rev Fluid Mech 2010;42(1):111–33.
[28] Corson J, Mulholland GW, Zachariah MR. Analytical expression for the friction coefficient of DLCA aggregates based on extended Kirkwood–Riseman theory. Aerosol Sci Technol 2017;51(6):766–77.
[29] Friedlander SK. Mass and heat transfer to single spheres and cylinders at low Reynolds numbers. AlChE J 1957;3(1):43–8.
[30] Macpherson GB. Molecular dynamics simulation in arbitrary geometries for nanoscale fluid mechanics [Ph.D. thesis]. University Of Strathclyde; 2008.
[31] Vance FH, Scholtissek A, Nicolai H, Hasse C. Flame propagation modes for iron particle clusters in air — part I: transition from continuous to discrete propagation mode under weak convection effects. Combust Flame 2024;260:113265.
[32] Thijs LC, Ramaekers WJS, Kuerten JGM, van Oijen JA, de Goey LPH. C. E. A. G. van Gool, Improvement of heat- and mass transfer modeling for single iron particles combustion using resolved simulations. Combust Sci Technol 2024;196(4):572–88.
[33] Israelachvili JN. Intermolecular and surface forces. Academic Press; 2011.
[34] Mora JFDL, Rosner DE. Effects of inertia on the diffusional deposition of small particles to spheres and cylinders at low Reynolds numbers. J Fluid Mech 1982;125:379–95.
[35] Mora JFDL, Rosner DE. Low Reynolds number capture of small particles on cylinders by diffusion, interception, and inertia at subcritical Stokes numbers. Aerosol Sci Technol 2019;53(6):647–62.
[36] von Smoluchowski M. Versuch einer mathematischen Theorie der Koagulationskinetik kolloider Lösungen. Zeitschrift fuer physikalische Chemie 1917;92:129–68.
[37] Gallier S, Braconnier A, Godfroy F, Halter F, Chauveau C. The role of thermophoresis on aluminum oxide lobe formation. Combust Flame 2021;228:142–53.